Applied Physics Letters

Acoustic impedance regulation of Helmholtz resonators for perfect sound absorption via roughened embedded necks

Cite as: Appl. Phys. Lett. **117**, 151904 (2020); https://doi.org/10.1063/5.0024804
Submitted: 11 August 2020 . Accepted: 01 October 2020 . Published Online: 14 October 2020

Mingyu Duan, Chenlei Yu, Zhimin Xu, Fengxian Xin, and Tian Jian Lu

Acoustic impedance regulation of Helmholtz resonators for perfect sound absorption via roughened embedded necks

Cite as: Appl. Phys. Lett. **117**, 151904 (2020); doi: 10.1063/5.0024804
Submitted: 11 August 2020 · Accepted: 1 October 2020 ·
Published Online: 14 October 2020

Mingyu Duan,[1,2] Chenlei Yu,[1,2] Zhimin Xu,[1,2] Fengxian Xin,[1,2,a)] and Tian Jian Lu[2,3,4,b)]

AFFILIATIONS

[1]State Key Laboratory for Strength and Vibration of Mechanical Structures, Xi'an Jiaotong University, Xi'an 710049, People's Republic of China
[2]MOE Key Laboratory for Multifunctional Materials and Structures, Xi'an Jiaotong University, Xi'an 710049, People's Republic of China
[3]State Key Laboratory of Mechanics and Control of Mechanical Structures, Nanjing University of Aeronautics and Astronautics, Nanjing 210016, People's Republic of China
[4]Nanjing Center for Multifunctional Lightweight Materials and Structures (MLMS), Nanjing University of Aeronautics and Astronautics, Nanjing 210016, People's Republic of China

[a)]Author to whom correspondence should be addressed: fengxian.xin@gmail.com
[b)]Electronic mail: tjlu@nuaa.edu.cn

ABSTRACT

Acoustic impedance regulation of a neck embedded Helmholtz resonator is realized by introducing surface roughness to the neck so as to convert the initially non-perfect sound absorber to a perfect sound absorber. The proposed roughened-neck embedded Helmholtz resonator (R-NEHR) achieves perfect sound absorption ($\alpha > 0.999$) at 158 Hz across a deep subwavelength thickness of $\lambda/42$. Theoretical predictions of the R-NEHR's performance are validated against experimental measurements. Physically, surface roughness triggers the periodic concentration effect of fluid vibration in the neck, thereby improving its acoustic mass and acoustic resistance and altering the resonant damping state of the absorber. As a result, the absorption peak position of the R-NEHR shifts by 16.0% to lower frequency, together with a peak value increase of 19.6%. This work provides an approach for perfect sound absorber design and impedance regulation of acoustic metamaterials.

Due to the long wavelength of low-frequency acoustic waves, it is difficult for traditional acoustic materials to realize effective absorption of low-frequency noise. Acoustic metamaterials can be resorted to address the issue. An acoustic metamaterial can realize a variety of fantastic properties by tailoring its microstructure, such as negative refraction,[1–4] acoustic focusing,[5–8] acoustic invisibility,[9–12] phase and amplitude modulation,[13] and high-performance selective sound silencing.[14] Based upon the classical Helmholtz resonators, it can also achieve low-frequency perfect sound absorption via coiled-up space,[15–18] multilayer series connection,[19–21] and neck embedded[22–24] design. However, as the realization of perfect sound absorption needs to strictly satisfy the condition of acoustic impedance matching, acoustic impedance regulation of the acoustic metamaterial becomes a crucial problem.

In this work, we realize acoustic impedance regulation of an imperfect neck embedded Helmholtz resonator (NEHR) in Fig. 1(a) by theoretical calculation and experimental measurement. Upon introducing surface roughness to the embedded neck, the proposed R-NEHR in Fig. 1(a) exhibits significantly enhanced acoustic impedance, resulting in tunable perfect sound absorption performance at low frequencies. The R-NEHR may thus be classified as a kind of acoustic metamaterial. We further analyze physical mechanisms underlying such performance improvement via impedance analysis, mesoscopic FEM simulation, and complex frequency plane analysis.

With reference to Fig. 1(a), the proposed acoustic metamaterial is formed by a cylindrical air cavity and an embedded neck. The NEHR has a neck in the form of a smooth hollow cylindrical tube, as shown in Fig. 1(b). As for the R-NEHR, periodic axial roughness of the neck is introduced to regulate its acoustic impedance. According to Fig. 1(c), the rough neck has an idealized cosinoidal inner surface characterized by a varying radius,[25,26] as

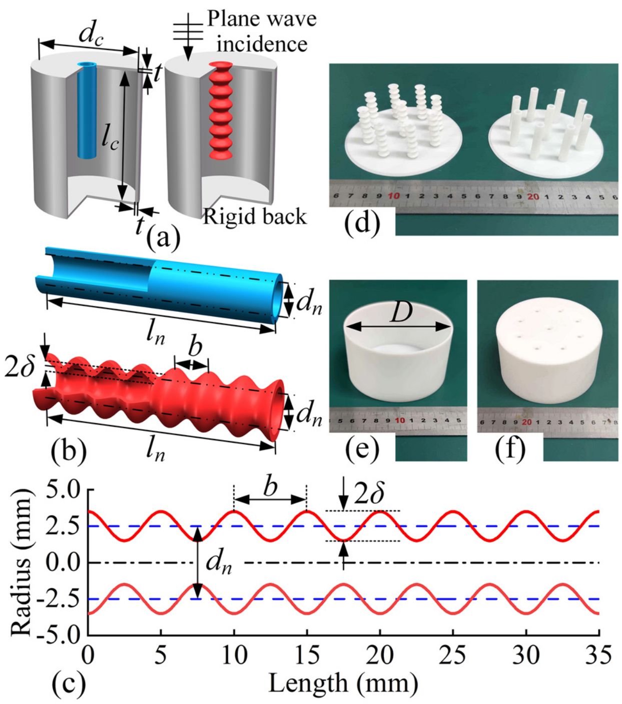

FIG. 1. (a) Schematic and working condition of the NEHR and R-NEHR with a cavity diameter of $d_c = 32$ mm, a facesheet thickness and a wall thickness of $t = 1$ mm, and a cavity depth of $l_c = 50$ mm. (b) Three-dimensional schematic of both smooth and rough necks with an inner diameter of $d_n = 5$ mm and a length of $l_n = 35$ mm. The rough neck is decorated by periodic axial roughness with a wavelength of $b = 5$ mm and a radial fluctuation of $\delta = 1$ mm on an average inner diameter of $d_n = 5$ mm. The above dimensions are chosen only to meet the processing accuracy for the manufacturing of test samples. The proposed method is actually not limited to the above special dimensions and has general applicability (see the supplementary material for details). (c) Two-dimensional schematic of the rough neck inner surface in a Cartesian coordinate system. (d) 3D-printed facesheet connected with nine smooth or rough necks having an identical perforation ratio as in (a). (e) 3D-printed cavity with an inner diameter of $D = \sqrt{9d_c^2} = 96$ mm. (f) The test sample obtained by bonding the facesheet of (d) to the cavity of (e).

$$\Gamma(x) = d_n[0.5 + \varepsilon \cos(\beta x)], \tag{1}$$

where $\varepsilon = \delta/d_n$ and $\beta = 2\pi d_n/b$ are defined as the relative roughness and the wavenumber of surface roughness and x is the position coordinate along the length of the neck, as shown in Fig. 1(c).

The acoustic wave excitation is considered as a plane wave incident vertically from the upper side of the acoustic metamaterial in Fig. 1(a). Acoustically, the bottom side of the metamaterial and the walls of both the cavity and embedded neck are taken as rigid. The sound absorption coefficient of the metamaterial can thus be calculated by[27]

$$\alpha = 1 - |R|^2 = 1 - \left| \frac{Z_s - 1}{Z_s + 1} \right|^2, \tag{2}$$

where R is the acoustic pressure reflection coefficient and Z_s is the surface acoustic impedance ratio of the metamaterial. Through appropriate regulation of Z_s, improved sound absorption of the metamaterial can be achieved.

For an air cavity with rigid backing, the acoustic impedance is given by[27]

$$Z_c = -jZ_0 \cot(\delta_1 k_0 l_c), \tag{3}$$

where j is the imaginary unit. $Z_0 = \rho_0 c_0$ is the characteristic impedance of air, where $\rho_0 = 1.29 \text{kg/m}^3$, $c_0 = 343$ m/s, and $k_0 = 2\pi f/c_0$ are the density, acoustic wave velocity, and wavenumber of air, and f is the acoustic wave frequency. $\delta_1 = [S_c l_c - S_n(l_n - t)]/(S_c l_c)$ is the depth correction factor considering the cavity volume occupied by the neck, and $S_c = \pi d_c^2/4$ and $S_n = \pi d_n^2/4$ are the cavity cross-sectional area and neck cross-sectional area, respectively. According to our previous work,[25,26,28] the tortuosity of the rough neck with cosinoidal axial roughness can be calculated by

$$\alpha_\infty = 1 + \frac{\varepsilon^2 \beta^2 \left[\left(J_0^2(\beta/2) \right) - \left(J_1^2(\beta/2) \right) \right]}{2J_1^2(\beta/2)}, \tag{4}$$

where J_n is the first kind modified Bessel function of the nth order. When the relative roughness $\varepsilon = 0$, Eq. (4) reduces to the tortuosity of a smooth neck, with $\alpha_\infty = 1$. Correspondingly, the static flow resistivity of the rough neck is given by[25,26,28]

$$\sigma_r = \sigma_s \left[\frac{1}{(1-2\varepsilon)^4} + \left(\frac{(6\varepsilon^2+1)}{(1-4\varepsilon^2)^{3.5}} - \frac{1}{(1-2\varepsilon)^4} \right) \frac{2e^{-\frac{1}{5\pi}\beta}}{1+e^{-\frac{1}{5\pi}\beta}} \right], \tag{5}$$

where $\sigma_s = 32\mu_0/{d_n}^2$ is the static flow resistivity of the smooth neck and $\mu_0 = 1.81 \times 10^{-5} \text{Pa} \cdot \text{s}$ is the dynamic viscosity of air. When $\varepsilon = 0$, Eq. (5) also reduces to the smooth case.

The acoustic impedance of the facesheet with a rough neck can be calculated using the model by Pride *et al.*,[29] as

$$Z_n = \left\{ \frac{\nu_0}{j\omega q_0} \left\{ 1 - \chi + \chi \left[1 + \left(\frac{8\alpha_\infty q_0}{3\Lambda} \right)^2 \frac{j\omega}{\nu_0} \right]^{1/2} \right\} + \alpha_\infty \right\} \rho_0 \omega j l_n, \tag{6}$$

where $\omega = 2\pi f$ is the angular frequency, $\nu_0 = \mu_0/\rho_0$ is the kinematic viscosity, $q_0 = \mu_0/\sigma_r$ is the viscous permeability, $\Lambda = \sqrt{8\mu_0\alpha_\infty/\sigma_r}$ is the viscous characteristic length, and $\chi = 3/4$ is the tortuous ratio of the axisymmetric neck. With end effects of the rough neck on acoustic mass and acoustic resistance accounted for, Z_n should be modified as[30]

$$Z_n{}' = Z_n + \frac{4\sqrt{2}\mu_0 y}{d_e} + 0.85 d_e j\omega\rho_0, \tag{7}$$

where $y = d_e\sqrt{\rho_0\omega/\mu_0}/2$ is the ratio of the neck end radius to viscous boundary layer thickness and $d_e = d_n(1+2\varepsilon)$ is the end diameter of the neck. Then, the surface acoustic impedance ratio of the metamaterial can be calculated as

$$Z_s = \delta_2 \left(Z_c + Z_n{}'/\varphi \right)/Z_0, \tag{8}$$

where $\varphi = S_n/S_c$ is the perforation ratio of the facesheet, $\delta_2 = A/S_c$ is the acoustic impedance correction factor considering the wall thickness of the cavity, and $A = \pi(d_c + 2t)^2/4$ is the cross-sectional area of the whole metamaterial. Finally, the sound absorption coefficient α can be calculated by substituting (7) into (2). Considering the neck roughness, the above theoretical model has actually extended the classical Maa's theory for smooth necks to rough necks.

To validate the foregoing theoretical predictions, test samples are manufactured via stereolithographic (SLA) 3D-printing with photosensitive resin. As shown in Fig. 1(d), the facesheet and the nine embedded necks, either smooth or rough, are printed as a whole. The perforation ratio of the facesheet is the same as that of Fig. 1(a). The facesheet and the 3D-Printed cavity shown in Fig. 1(e) are subsequently bonded to form the sample shown in Fig. 1(f). The acoustic impedance and sound absorption coefficient of the samples are measured with the Brüel & Kjær impedance tube according to ASTM standard[31] (see the supplementary material for details), as shown in Fig. 2(a).

The theoretically calculated sound absorption coefficient and acoustic impedance of both the NEHR and R-NEHR are compared with experimental measurements in Figs. 2(b)–2(d). Good agreement is achieved, especially for the peak value and peak position of the sound absorption coefficient. From Fig. 2(b), it is found that the sound absorption coefficient of the NEHR, shown as the blue curve and blue circles, reaches a peak value of 0.83 at 188 Hz and, hence, perfect absorption is not achieved. In sharp contrast, the R-NEHR with roughened neck realizes perfect sound absorption at 158 Hz, with a peak value of $\alpha > 0.999$ (measured by experiment). Therefore, introducing surface roughness to the neck causes significant improvement in low-frequency sound absorption performance. Specifically, the absorption peak value is increased by 19.6% (from 0.83 to 0.999), and the peak frequency is shifted to a lower frequency, with a decrease in 30 Hz (16.0% drop). As a result, the proposed R-NEHR realizes low-frequency perfect absorption with a deep subwavelength thickness of 51 mm or 1/42 of the corresponding acoustic wavelength. The significant performance improvement is attributed to acoustic impedance regulation via roughened neck. Actually, this improvement can be achieved on acoustic metamaterials of any dimension. For different applications, metamaterials of different thicknesses can be designed by introducing neck roughness to achieve perfect absorption for different frequencies on the deep subwavelength scale (see the supplementary material for details).

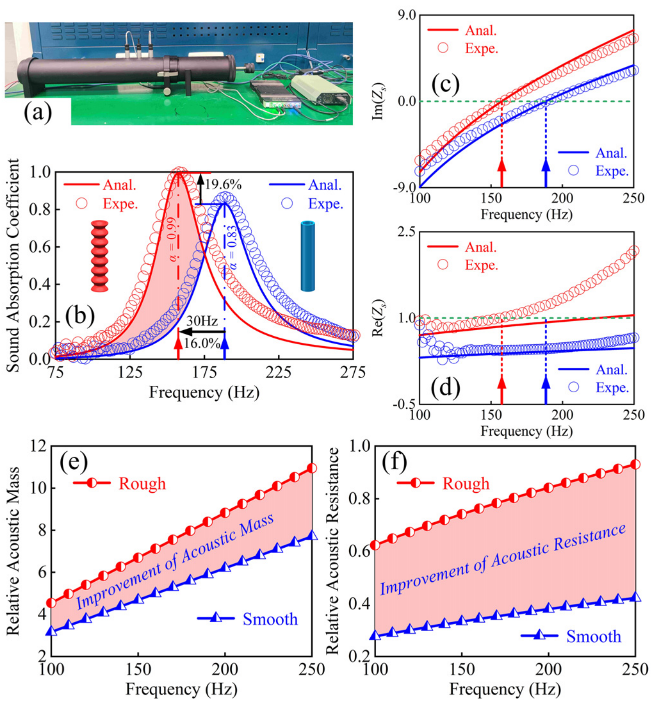

FIG. 2. Acoustic performance comparison between the NEHR and R-NEHR. (a) Experimental setup of B&K 4026A impedance tube. (b) Sound absorption coefficient, (c) surface acoustic reactance ratio, and (d) surface acoustic resistance ratio obtained by the theoretical calculation and experimental measurement. Blue and red arrows indicate the sound absorption peak frequency of the NEHR and R-NEHR. (e) Relative acoustic mass and (f) relative acoustic resistance of the smooth neck and rough neck.

From Eqs. (4) and (5), it can be seen that the relative roughness ε and wavenumber β of the neck roughness can determine the tortuosity α_∞ and the static flow resistivity σ_r of the neck. According to Eqs. (6) and (7), the changes of the tortuosity and the static flow resistivity lead to the change of the acoustic impedance of the metamaterial. Therefore, the introduction of the roughness provides additional tunable degrees of freedom for acoustic performance, and the above sound absorption enhancement is actually achieved by adjusting the roughness to regulate the acoustic impedance of the metamaterial to meet the impedance matching condition. The theoretically calculated imaginary part of Z_s (i.e., surface acoustic reactance ratio) and real part of Z_s (i.e., surface acoustic resistance ratio) are compared with those measured in Figs. 2(c) and 2(d), respectively. According to Eq. (2), the impedance matching condition dictates that perfect absorption can only be achieved when $\mathrm{Im}(Z_s) = 0$ and $\mathrm{Re}(Z_s) = 1$ are realized simultaneously. Since $\mathrm{Im}(Z_s)$ and $\mathrm{Re}(Z_s)$ are not independent variables, such a condition is often not strictly satisfied. Generally speaking, at relatively low frequencies, the absolute value of $\mathrm{Im}(Z_s)$ is higher than that of $\mathrm{Re}(Z_s)$ so that the absorption peak frequency is usually determined by the zero of $\mathrm{Im}(Z_s)$ and the absorption peak value is determined by the damping state controlled by $\mathrm{Re}(Z_s)$. From Fig. 2(c), it is seen that, with the regulation of acoustic impedance, $\mathrm{Im}(Z_s)$ of the R-NEHR is higher than that of the NEHR in the frequency band studied, causing $\mathrm{Im}(Z_s)$ to reach zero at a lower frequency. As a result, the metamaterial achieves a lower resonant frequency. Also, $\mathrm{Re}(Z_s)$ of the R-NEHR is improved compared with the NEHR, as shown in Fig. 2(d). At the resonant frequency, $\mathrm{Re}(Z_s)$ of the R-NEHR is much closer to 1 than that of the NEHR. Consequently, the NEHR falls within the under damping state at the resonant frequency, while the R-NEHR is in the critically damping state and satisfies the impedance matching condition. Therefore, the proposed R-NEHR can realize perfect sound absorption.

The acoustic impedance of the present acoustic metamaterial is actually composed of the acoustic capacitance of the air cavity and the acoustic mass and acoustic resistance of the embedded neck. Since the NEHR and the R-NEHR have the same cavity, we additionally analyze how the neck differs before and after roughness is introduced. The imaginary and real parts of Z_n/Z_0 are defined as the relative acoustic mass and relative acoustic resistance of the neck, which are plotted in Figs. 2(e) and 2(f). Upon introducing the roughness, significant improvement occurs in both the acoustic mass and acoustic resistance of the neck. This is the fundamental principle of acoustic impedance regulation. If we analogize the R-NEHR as a spring-oscillator system, according to the theory of vibration,[32] a higher acoustic mass and a larger acoustic resistance result in lower resonance frequency and more energy dissipation of the metamaterial, respectively.

To explore physical mechanisms underlying acoustic mass and acoustic resistance improvement of the rough neck at a mesoscopic level, we establish a finite element (FE) model in COMSOL[33] (see the supplementary material for details). The distribution of particle vibration velocity in the rough neck is selected from the overall model for analysis and compared with that in the smooth neck, as shown in Figs. 3(a) and 3(b). The spatial average of vibration velocity on the cross section of the neck along its length is calculated and plotted in Fig. 3(c). The vibration velocity in the smooth neck is seen to be uniformly distributed, with a value of about 0.15 m/s for the parameters selected. However, in the rough neck, the average vibration velocity varies periodically along the neck length. The periodic concentration effect of fluid vibration is observed at each of the narrow sections, where the maximum vibration velocity exceeds 0.35 m/s, for surface roughness changes fluid flow characteristics in the neck. The periodic concentration effect obstructs fluid flow, thereby enlarging the acoustic mass of the rough neck at the macro level.

The acoustic energy dissipation density in the smooth neck is compared with that in the rough neck in Figs. 3(d) and 3(e). Energy dissipation in the former mostly occurs nearby its inner wall, with little energy dissipation occurring at its center. Furthermore, according to the cross-sectional energy dissipation density along the neck length shown in Fig. 3(f), energy dissipation in the smooth neck is stable at 2.14×10^{-5} W/m. In sharp contrast, energy dissipation in the latter exhibits the same periodic variation trend as that of vibration velocity along the neck length. Due to the periodic concentration effect of vibration velocity, the concentration of high level vibration velocity at each narrow section of the rough neck causes intense friction between fluid and the inner surface of the neck, causing the intense energy dissipation shown in Fig. 3(e). Thus, the rough neck shows superior energy dissipation performance, which is manifested as its enlarged acoustic resistance macroscopically. It can thus be concluded that the introduction of surface roughness triggers the periodic concentration effect of vibration velocity, by which the acoustic mass and acoustic resistance of the neck are enlarged so that acoustic impedance regulation can be realized.

We further analyze how roughness affects the sound absorption performance and damping state of the R-NEHR with relevant geometric parameters fixed. From Fig. 4(a), as the relative roughness ε is increased from 0 (i.e., the smooth case) to 0.25, the sound absorption peak of the R-NEHR is increasingly shifted to lower frequencies, with the peak value increasing correspondingly from 0.83 to perfect absorption. When $0.20 < \varepsilon < 0.25$, the R-NEHR exhibits a tunable perfect absorption ability. With complex frequency plane analysis[34] of the reflection coefficient $|R|^2$, the damping state of the R-NEHR is investigated to explain the effect of neck roughness, as shown in Figs. 4(b)–4(e). By replacing the frequency f in the previous theoretical prediction model with a complex frequency as $f' = f_{re} + jf_{im}$ (f_{re} and f_{im} are the real frequency and imaginary frequency, respectively), the reflection coefficient $|R|^2$ can be plotted in the complex frequency plane with f_{re} and f_{im} as variables. In a lossless system, the reflection coefficient has a pair of complex conjugate zero and pole points, where the complex number is related to the energy leakage of the radiation. The zero and pole points in the complex frequency plane represent the minimum value ($|R|^2 = 0$, i.e., complete absorption) and maximum value of the reflection coefficient, respectively. In a lossy system, the introduction of loss causes the zero and pole points shift simultaneously. When the zero just falls on the real frequency axis (i.e., $f_{im} = 0$), the losses completely balance the energy leakage and satisfy the critical coupling condition for complete absorption. Figures 4(b)–4(e) display the values of $|R|^2$ expressed in the complex frequency plane with various relative roughness ε. When $\varepsilon = 0$, the

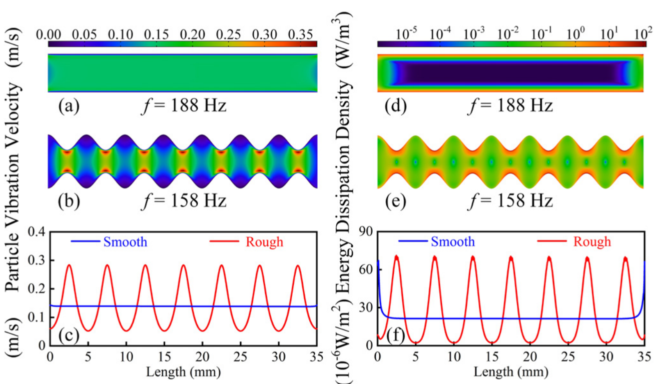

FIG. 3. (a) and (b) Distribution of particle vibration velocity in smooth and rough necks at absorption peak frequencies. (c) Average particle vibration velocity at the cross section of smooth and rough necks along the neck length. (d) and (e) Distribution of acoustic energy dissipation density in smooth and rough necks at absorption peak frequencies. (f) Acoustic energy dissipation of the cross section in smooth and rough necks along the neck length.

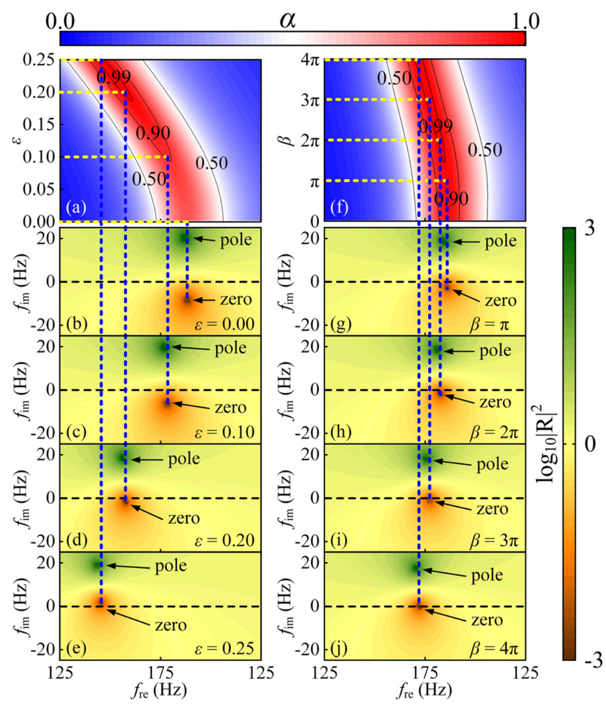

FIG. 4. (a) Sound absorption spectrum of the R-NEHR with frequency and relative roughness as variables. (b)–(e) Complex frequency plane analysis for the reflection coefficient of the R-NEHR for selected values of relative roughness. (f) Sound absorption spectrum of the R-NEHR with frequency and wavenumber as variables. (g)–(j) Complex frequency plane analysis for the reflection coefficient of the R-NEHR for selected values of wavenumbers. (a), (b), (c), and (d) share the same x-axis as (e), while (f), (g), (h), and (i) share the same x-axis as (j).

vibration velocity does not have the periodic concentration effect, and so the acoustic mass and acoustic resistance of the neck remain at a relatively low level. The losses are not sufficient to balance the energy leakage, causing the zero of $|R|^2$ to stay below the real frequency axis in Fig. 4(b). As a result, the metamaterial falls within the under damping state and perfect absorption cannot be realized. With the increase in ε, the periodic concentration effect occurs and becomes increasingly more significant, which enlarges the acoustic mass and acoustic resistance. According to the results of Figs. 4(c) and 4(d), the zero and pole shift to the up and left, and the zero almost falls on the real frequency axis when $\varepsilon = 0.2$. The R-NEHR is transitioned into a critical damping state so as to realize impedance matching and perfect absorption. If the value of relative roughness ε continues to increase on this basis, the zero will eventually cross the real frequency axis and stay above it, leading to an over damping state, as shown in Fig. 4(e).

The effect of wavenumber β on sound absorption is presented in Fig. 4(f). Increasing the value of β can also shift the absorption peak frequency to a lower frequency accompanied by an enlarged peak value. Due to the existence of ε, the periodic concentration effect is always present during the variation of β. Thus, the improvement of β on the periodic concentration effect is not as evident as ε. According to Figs. 4(g)–4(j), the zero and pole mainly shift to the left as β is increased, causing the resonant sound absorption frequency to decrease. Furthermore, the zero is shifted from below the real frequency axis to that on the axis in the vertical direction, causing the R-NEHR to transit from the under damping state to the critically damping state. In conclusion, for the R-NEHR, increasing its neck roughness can intensify the periodic concentration effect and cause the transition of its resonant damping state. Based on this principle, the acoustic impedance of the R-NEHR can be regulated to an impedance matching state so as to realize tunable perfect sound absorption.

In summary, we propose a unique method to improve the sound absorption performance and regulate the acoustic impedance of acoustic metamaterials via introducing roughness. Upon introducing surface roughness to the embedded necks of Helmholtz-type resonators, the periodic concentration effect of vibration velocity in the neck is triggered. This effect enlarges acoustic mass and acoustic resistance of the neck, thus enabling acoustic impedance regulation. Tailoring the neck roughness can lead to the transition of the damping state of the metamaterial to the critically damping state so as to achieve impedance matching and tunable perfect absorption at low frequencies (by the deep subwavelength scale). This work enriches the design methods of acoustic metamaterials and has important guiding significance for the development of acoustic metamaterials.

See the supplementary material for the effect of the thickness on acoustic metamaterials performance, the finite element model, and the experimental method.

This work was supported by the NSFC (Nos. 11761131003, 52075416, U1737107, and 11772248) and the Open Fund of the State Key Laboratory of Mechanics and Control of Mechanical Structures (Nos. MCMS-I-0219K01 and MCMS-E-0219K02).

DATA AVAILABILITY

The data that support the findings of this study are available from the corresponding author upon reasonable request.

REFERENCES

[1] J. Li and C. T. Chan, Phys. Rev. E **70**, 055602 (2004).
[2] R. Zhu, X. N. Liu, G. K. Hu, C. T. Sun, and G. L. Huang, Nat. Commun. **5**, 5510 (2014).
[3] N. Kaina, F. Lemoult, M. Fink, and G. Lerosey, Nature **525**, 77 (2015).
[4] S. Tong, C. Ren, and W. Tang, Appl. Phys. Lett. **114**, 204101 (2019).
[5] S. Zhang, L. Yin, and N. Fang, Phys. Rev. Lett. **102**, 194301 (2009).
[6] C. Shen, Y. Xie, N. Sui, W. Wang, S. A. Cummer, and Y. Jing, Phys. Rev. Lett. **115**, 254301 (2015).
[7] R. Al Jahdali and Y. Wu, Appl. Phys. Lett. **108**, 031902 (2016).
[8] S. Qi, Y. Li, and B. Assouar, Phys. Rev. Appl. **7**, 054006 (2017).
[9] H. Chen and C. T. Chan, Appl. Phys. Lett. **91**, 183518 (2007).
[10] B. I. Popa, L. Zigoneanu, and S. A. Cummer, Phys. Rev. Lett. **106**, 253901 (2011).
[11] L. Zigoneanu, B. I. Popa, and S. A. Cummer, Nat. Mater. **13**, 352 (2014).
[12] Z. Sun, X. Sun, H. Jia, Y. Bi, and J. Yang, Appl. Phys. Lett. **114**, 094101 (2019).
[13] R. Ghaffarivardavagh, J. Nikolajczyk, R. G. Holt, S. Anderson, and X. Zhang, Nat. Commun. **9**, 1349 (2018).
[14] R. Ghaffarivardavagh, J. Nikolajczyk, S. Anderson, and X. Zhang, Phys. Rev. B **99**, 024302 (2019).
[15] F. Wu, Y. Xiao, D. Yu, H. Zhao, Y. Wang, and J. Wen, Appl. Phys. Lett. **114**, 151901 (2019).
[16] H. Long, C. Shao, C. Liu, Y. Cheng, and X. Liu, Appl. Phys. Lett. **115**, 103503 (2019).
[17] K. Donda, Y. Zhu, S.-W. Fan, L. Cao, Y. Li, and B. Assouar, Appl. Phys. Lett. **115**, 173506 (2019).
[18] Y. Shen, Y. Yang, X. Guo, Y. Shen, and D. Zhang, Appl. Phys. Lett. **114**, 083501 (2019).
[19] Y. Tang, F. Li, F. Xin, and T. J. Lu, Mater. Des. **134**, 502 (2017).
[20] Y. Tang, S. Ren, H. Meng, F. Xin, L. Huang, T. Chen, C. Zhang, and T. J. Lu, Sci. Rep. **7**, 43340 (2017).
[21] Y. Tang, F. Xin, L. Huang, and T. Lu, Europhys. Lett. **118**, 44002 (2017).
[22] S. Huang, X. Fang, X. Wang, B. Assouar, Q. Cheng, and Y. Li, J. Acoust. Soc. Am. **145**, 254 (2019).
[23] S. Huang, X. Fang, X. Wang, B. Assouar, Q. Cheng, and Y. Li, Appl. Phys. Lett. **113**, 233501 (2018).
[24] S. Huang, Z. Zhou, D. Li, T. Liu, X. Wang, J. Zhu, and Y. Li, Sci. Bull. **65**, 373 (2020).
[25] S. Song, X. Yang, F. Xin, and T. J. Lu, Phys. Fluids **30**, 023604 (2018).
[26] Z. Xu, X. Peng, X. Liu, F. Xin, and T. J. Lu, Europhys. Lett **125**, 34004 (2019).
[27] J. F. Allard and N. Atalla, *Propagation of Sound in Porous Media: Modelling Sound Absorbing Materials*, 2nd ed. (John Wiley & Sons, Ltd., 2009).
[28] Z. Xu, S. Song, F. Xin, and T. J. Lu, Phys. Fluids **31**, 013602 (2019).
[29] S. R. Pride, F. D. Morgan, and A. F. Gangi, Phys. Rev. B **47**, 4964 (1993).
[30] D. Maa, Sci. Sin. **18**, 55 (1975).
[31] ASTM E1050-2012. "Standard test method for impedance and absorption of acoustical materials using a tube, two microphones and a digital frequency analysis system" (ASTM, 2012).
[32] H. Kuttruff, *Acoustics: An Introduction* (CRC Press, 2006).
[33] J. Zhong, H. Zhao, H. Yang, J. Yin, and J. Wen, Appl. Acoust. **145**, 104 (2019).
[34] V. Romero-Garcia, G. Theocharis, O. Richoux, and V. Pagneux, J. Acoust. Soc. Am. **139**, 3395 (2016).